Received: 10 July 2023 | Revised: 12 August 2023 | Accepted: 15 August 2023

DOI: 10.1002/agt2.409

Aggregate Open Access WILEY

RESEARCH ARTICLE

Microfluidic bubble-generator enables digital light processing 3D printing of porous structures

Philipp Weber[1] | **Ling Cai**[1] | **Francisco Javier Aguilar Rojas**[1] | **Carlos Ezio Garciamendez-Mijares**[1] | **Maria Celeste Tirelli**[2] | **Francesco Nalin**[2] | **Jakub Jaroszewicz**[3] | **Wojciech Święszkowski**[3] | **Marco Costantini**[2] | **Yu Shrike Zhang**[1]

[1]Division of Engineering in Medicine, Department of Medicine, Brigham and Women's Hospital, Harvard Medical School, Cambridge, Massachusetts, USA

[2]Institute of Physical Chemistry—Polish Academy of Sciences, Kasprzaka, Poland

[3]Biomaterials Group, Materials Design Division, Faculty of Materials Science and Engineering, Warsaw University of Technology, Woloska, Poland

Correspondence
Wojciech Święszkowski, Biomaterials Group, Materials Design Division, Faculty of Materials Science and Engineering, Warsaw University of Technology, Woloska, Warsaw, Poland.
Email: wojciech.swieszkowski@pw.edu.pl

Marco Costantini, Institute of Physical Chemistry—Polish Academy of Sciences, Kasprzaka, Warsaw, Poland.
Email: mcostantini@ichf.edu.pl

Yu Shrike Zhang, Division of Engineering in Medicine, Department of Medicine, Brigham and Women's Hospital, Harvard Medical School, Cambridge, MA, USA.
Email: yszhang@bwh.harvard.edu

Funding information
National Science Centre Poland (NCN), Grant/Award Number: 2020/37/B/ST8/02167; European Union's Horizon 2020 research and innovation program, Grant/Award Number: 813786; National Institutes of Health, Grant/Award Number: R21EB025270; National Science Foundation, Grant/Award Number: CBET-EBMS-1936105; Brigham Research Institute

Abstract

Three-dimensional (3D) printing is an emerging technique that has shown promising success in engineering human tissues in recent years. Further development of vat-photopolymerization printing modalities has significantly enhanced the complexity level for 3D printing of various functional structures and components. Similarly, the development of microfluidic chip systems is an emerging research sector with promising medical applications. This work demonstrates the coupling of a digital light processing (DLP) printing procedure with a microfluidic chip system to produce size-tunable, 3D-printable porosities with narrow pore size distributions within a gelatin methacryloyl (GelMA) hydrogel matrix. It is found that the generation of size-tunable gas bubbles trapped within an aqueous GelMA hydrogel-precursor can be controlled with high precision. Furthermore, the porosities are printed in two-dimensional (2D) as well as in 3D using the DLP printer. In addition, the cytocompatibility of the printed porous scaffolds is investigated using fibroblasts, where high cell viabilities as well as cell proliferation, spreading, and migration are confirmed. It is anticipated that the strategy is widely applicable in a range of application areas such as tissue engineering and regenerative medicine, among others.

KEYWORDS
3D printing, biofabrication, bubble, digital light processing, microfluidics, porous

1 | INTRODUCTION

The development of novel three-dimensional (3D) printing modalities for the fabrication of biological scaffolds has risen extensively in recent decades.[1–3] In addition, the use of 3D cell culturing has shown to have significant advantages in terms of mimicking the native tissues when compared to the conventional two-dimensional (2D) cell cultivations.[4–6] To further complement and optimize 3D cell cultivation, past reports have suggested that porous scaffolds can benefit cell behaviors. For example, it has been demonstrated that cell proliferation, spreading, migration as well as cell differentiation can be enhanced by the presence of void volumes; in addition, porous scaffolds provide higher diffusion rates,

Philipp Weber and Ling Cai contributed to this work equally.

which in turn, improve cell ingrowth, transport of bioactive agents, or removal of cell metabolites.[7–12]

Porous 3D constructs can already be manufactured in a variety of ways.[13–15] One common approach is to use salt or microspheres, which serve as placeholders of the void volume, and which are entrapped in a photocrosslinkable polymer matrix.[16–20] Despite its success, this procedure has some drawbacks, such as being a time-consuming approach involving multiple steps to dissolve away the porogen, or being incompatible with 3D printing operations. Additional reports utilized other sacrificial components such as inert solvent introduced into the ink.[21] Subsequently, postprinting, the sacrificial components are removed through washing, resulting in the fabrication of 3D-printed porous structures. Yet similarly, the necessary postprinting processing would require the continuous phases to be present for efficient removal of the sacrificial components and may thus reduce the fabrication efficiency and flexibility.

To this end, it has been demonstrated how such a complex process of producing porous structures can be significantly accelerated using microfluidic chips. For instance, a valve-based flow-focusing (vFF) chip made from biocompatible materials was used to produce gas bubbles with precisely adjustable diameters and narrow size distributions, which were trapped in a polymer matrix.[22,23] The polymer matrix can subsequently be crosslinked via various methods. The use of the reported microfluidic chip thus enables, compared to other established methods for the generation of porosities such as microsphere templating, the production of porous scaffolds in a simpler, faster, and more controllable way. At the same time, uniform pore size distributions can be provided with a simple set of process parameters in a robust manner.

As this approach was so far only utilized for extrusion 3D printers,[22] there is a reasonable conjecture to further improve the process using a 3D digital light processing (DLP) printing platform as a first proof-of-concept. Even though extrusion-based 3D printing is simple to operate, it oftentimes is less efficient when fabricating volumetric constructs featuring sophisticated internal architectures and external shapes.[24] In comparison, vat-polymerization-based 3D printing, with its advantage of rapid crosslinking, facilitates the efficient construction of 3D porous structures.[25,26] Existing research has further revealed that grating-based laser-assisted stereolithography apparatus (SLA) printing technology requires high maintenance costs for the gratings and has slower curing speeds compared to the surface projection-based DLP technology when constructing 3D scaffolds.[27,28] Therefore, the development of DLP-based 3D printing of porous structures is a promising strategy.

While DLP printing allows convenient generation of complex patterns in both 2D and 3D,[29–31] its vat setup also potentially enables seamless integration with microfluidic devices towards streamlined operations.[32–34] We thus hypothesized that with the microfluidic bubble-generator, when combined with the DLP system, it is possible to further enhance our capability in producing in a single step, porous scaffolds with geometrically sophisticated structures, for relevant applications. Accordingly, the 3D printing process developed in this work may contribute to the state-of-the-art as there are currently few methods that allow the fabrication of size-tunable pores over a wide range within a single 3D-printed biocompatible construct.

Figure 1 illustrates the main components used in this work. Figure 1A schematically shows the microfluidic vFF chip, as a photograph and as a microscopic image of the junction point. Basically, the gas and polymer solution meet upstream the flow focusing junction, resulting in the rapid generation of a foam where the size of the dispersed gas bubbles can be precisely adjusted. Figure 1B shows the rendering of the 3D DLP top-down printer. Here, the biphasic ink to be printed is directly introduced from the vFF chip into an ink vat whereas the printing stage is embedded into it. In contrast to bottom up DLP printers, the light source illuminates from the above, and the printing stage is immersed in the vat by one layer thickness with each additional layer being printed and stage moved downward, eliminating the potential negative effect of gravitational force.[29,31] This process is further illustrated in Figure 1B using the example of a printed bone-like structure.

2 | MATERIALS AND METHODS

2.1 | Synthesis of GelMA

For each batch of fish-derived GelMA (fGelMA; Sigma-Aldrich), a 10% (w/v) solution of gelatin (from cold-water fish skin) in Dulbecco's phosphate-buffered saline (DPBS; Thermo Fischer Scientific) was prepared following a standard procedure.[35–37] Once gelatin was fully dissolved, 12 mL of methacrylic anhydride (MAA; Sigma-Aldrich) per 100 mL was added dropwise to the fish gelatin solution. This reaction was stirred at 50°C for 2 h. Preheated DPBS was used to stop the reaction by diluting the fGelMA solution after its reaction time. To remove unreacted, conceivably cytotoxic MAA, the fGelMA solution was dialyzed using 12–14-kDa cutoff dialysis membranes (Spectrum Laboratories) at a five-fold water excess. For that, the solution was dialyzed at 40°C for 5 days. Excess water is changed twice a day. After dialysis, the fGelMA solution was vacuum-filtered using 0.22-μm filter membranes (Sigma-Aldrich). Subsequently, the fGelMA solutions were stored at −80°C before finally lyophilizing them for 5 days at <0.150 mbar and 40°C.

2.2 | Synthesis of rhodamine-conjugated GelMA

The synthesis of red fluorescent fGelMA was taken from the literature.[38,39] First, an activation solution consisting of 0.1-g rhodamine B (Sigma-Aldrich) was dissolved in 10 mL of *N,N*-dimethyl formamide (Sigma-Aldrich) (DMF). Then, 0.12 g of N-hydroxysuccinimide (NHS; Sigma-Aldrich) and 0.2 g of (1-ethyl-(3-dimethylaminopropyl) carbonic diimide hydrochloride (EDC; Sigma-Aldrich) were added successively. This reaction was conducted under stirring for 4 h at room temperature. 1 g of freeze-dried fGelMA was dissolved in 20 mL of DPBS and 1 mL of the previously prepared activation solution was added dropwise at 37°C. This conjugation was continued for 24 h in the dark at 37°C. The resulting solution was transferred into dialysis membranes and dialyzed in deionized (DI) water at 37°C until no colored residue was visible in the dialysis water. Afterwards,

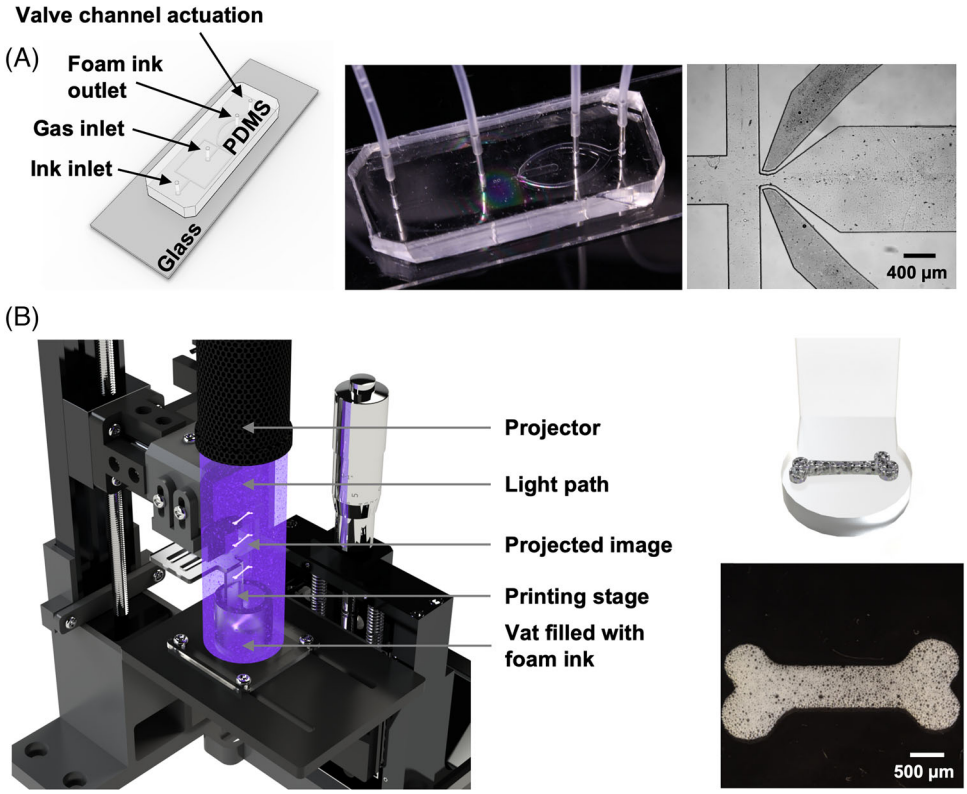

FIGURE 1 (A) Illustration of the valve-based flow-focusing (vFF) chip highlighting its two gas inlets, one ink inlet, and the outlet for the generated bubbles. (B) Schematic close-up rendering of the developed digital light processing (DLP) top-down 3D printer, where the printing stage was inserted into the vat with the light illuminating from the projector onto the printing stage. The right images present a schematic print of a bone-like structure on top of the printing stage (top), and a real print of this bone-like porous structure (bottom).

the solution was frozen at −80°C before freeze-drying it at <150 mbar and 40°C for 5 days.

2.3 | Microfabrication of vFF chips

The master of the chip was created on a silicon wafer using standard photolithography.[40] The wafer was coated with SU8-2150 (Microchem Corp., USA) by spinning it at 3500 rpm for 30 s. The chip was then soft-baked at 65°C for 5 min and at 95°C for 25 min, before being exposed through a high-precision photolithography mask. Postexposure baking was carried out at 65°C for 5 min, and 95°C for 11 min. Then, the master was immersed in SU8-developer for 15 min to remove the unexposed SU8. After developing, the chip was hard-baked at 195°C for 5 min, and finally obtained a master with features of approximately 135 μm. Finally, the master was silanized to avoid sticking of the polydimethylsiloxane (PDMS) on the SU8 features by placing the master in a vacuum chamber with 30 μL of silane (trichloro(1H, 1H, 2H, 2H-perfluorooctyl)silane, Sigma-Aldrich), and activating the pump for 45 min at 10 mbar (Figure S1).

To increase the flexibility of the membranes, we prepared PDMS-precursor (Sylgard 184, Dow Corning) with 20:1 w/w ratio of base to curing agent. One drop of the 20:1 PDMS-precursor was disposed on the cross junction of the flow focusing, and baked it for 30 min at 70°C. After this initial step, we further covered the whole master with the 10:1 PDMS-precursor and baked for additional 2 h at 70°C. The cured PDMS was peeled off the master, punched for the inlets of the chip, and standard plasma-bonding with a clean glass slide was performed.[41]

2.4 | Preparation of porous hydrogels

Lyophilized fGelMA was prepared with a concentration of 7.5% (w/v) in DI water. To reduce the surface tension of the solution and thus to improve the stability of the foam over the printing duration, three different surface-active agents (surfactants) were tested: rhamnolipids (AGAE Technologies), cetrimonium bromide (CTAB; Sigma-Aldrich), and soybean-derived lecithin (Alfa Aesar). These were added at varying concentrations of 0.5% and 5% (w/v). The corresponding ink was added to the vFF chip at a flow rate of 650 μL min^{-1} using a syringe pump (New Era Pump Systems Inc.) and a pressure p_g of 1.3 bar using a multi-stage pressure regulator. The pressure p_v applied to the vFF orifice was kept at atmospheric pressure. The resulting foam was transferred into a vial and the stability of the foam was assessed over a period of 5 min upon visual observation at room temperature. The most stable solution among these three surfactants was then observed again at concentrations ranging from 0–5% (w/v) over a period of 5 min to determine the most stable surfactant concentration.

To make the hydrogel photocrosslinkable, a photoinitiator was added to the solution. For this, varying concentrations of the photoinitiator lithium phenyl-2,4,6-trimethylbenzoylphosphonate (LAP; Sigma-Aldrich) were tested in 2D experiments. The concentrations were 0.2%, 0.4%, and 1% (w/v). The mixtures were introduced into the

vFF chip at a flow rate of 650 μL min^{-1} via a syringe pump. The applied pressure p_g was 1.3 bar, whereas the applied pressure at the orifice p_v remained at atmospheric pressure. The resulting foam was dispensed onto a glass slide and then crosslinked for different time intervals at 405-nm light with a minimum system output power of 700 mW.

2.5 | Bubble-generation within the microfluidic vFF chip

Since the use of microfluidic systems requires very small and precise volumetric flow rates as well as gas pressures, a self-built pressure regulator was used to control the gas flow into the vFF chip gas inlet p_g. The system is shown in Figure S2, highlighting its main components. To utilize it, filtered air was supplied to the pressure regulator via a compressed gas tank with a single-stage pressure regulator. Built into the pressure regulator was a solenoid valve, which was controlled by an Arduino UNO, and which delivered a positive pressure to its gas outlet using a proportional-integral-derivative (PID) controller connected to a pressure sensor. To quickly set a constantly precise pressure at the pressure regulator outlet, the PID gain factors were set to $k_P = 2.0$, $k_I = 0.0119$, and $k_D = 0.0$. These values were set based on experience and were examined in pretrials.

To generate size-tunable gas bubbles trapped inside of the hydrogel, the volumetric flow rate of the ink was adjusted using a syringe pump. The ink was then fed into the ink inlet of the vFF chip. For the use of the pressure regulator in connection with the vFF chip, the pressure inlet of the pressure regulator was connected to a tank with compressed gas, whereas the outlet was attached to the gas inlet p_g of the vFF chip. To adjust the inlet pressure, simply the target value was manually set using the potentiometer and its related display (Figure S2). To control the width of the orifice, a second gas tank was connected to the corresponding orifice of the vFF chip, p_v, via an analog multi-stage pressure regulator.

During the experiments, different combinations of volumetric flow rates of the ink as well as different pressures p_g supplied via the pressure regulator were tested. These were used to determine the most robust combinations possible for generating bubbles of varying diameters. Subsequently, the influence of the orifice width on the formation of the bubbles was observed as well. For the optical analysis of the bubble-generation inside the vFF chip, it was placed under a bright-field microscope where the bubble-generation was observed. All experiments were performed at room temperature to avoid fluctuations in terms of viscosity and consequently bubble-generation.

3 | 2D DLP PRINTING

The preferred ink composition consisting of set amounts of fGelMA, surfactant, and photoinitiator was further used to generate 2D structures with size-tunable pores. For this, the produced foam with varying bubble sizes, corresponding to the most robust combination of volumetric flow rate and the two applied pressures p_g and p_v on the vFF chip, was placed on a glass slide. After crosslinking, the 2D prints were analyzed via microscopic imaging to generate quantitative data on the uniformity of the different bubble sizes.

To demonstrate the X-Y resolution of the DLP prints, lines with decreasing widths were crosslinked in 2D. For this purpose, the same process as previously described was applied, to determine whether and to what extent the X-Y resolution of the DLP print depends on the bubble size. For this investigation, on the one hand, prints were made in which no bubbles were present within the ink. On the other hand, the smallest and largest bubbles which were achieved in the experiments were examined.

4 | 3D DLP PRINTING

The components and the structural set-up of the top-down printer used in this work are illustrated in Figure 1. The installed UV projector was a PRO4500 (Wintech) with a lens with 92-mm working distance. The exact wavelength as well as the intensity of the light was adjustable by the software LightCrafter4500 (Texas Instruments). This offered the possibility to use different photoinitiator systems or to control the light penetration depth via the set intensity. According to the manufacturer, the projector used provides a minimum system output power of 700 mW for 405-nm UV light. To use the printer properly, the printing stage was recalibrated and put back into focus for each new print as the vat was being moved in z-axis every time. This was done automatically by a built-in sensor. The printing stage of the top-down printer was circular with a diameter of 1 cm, while the vat was cylindrical and had a diameter of 1.5 cm and a height of 2 cm (Figure 1).

To control the motor moving the printing stage on the printing systems, an Arduino Mega micro-controller was connected between the motor and the operating computer. The corresponding in-house-written code for the coupling of both devices was applied using the open-source software Arduino IDE. The software used to control the movement of the printing stage was also an in-house-written code that operated via MATLAB (Mathworks) and that was equipped with a graphical-user interface (GUI). Through this software, it was possible to slice standard tessellation language (STL) files for 3D printing, as well as set the printing parameters and run 3D prints.

4.1 | Preparation of microcomputed tomography samples

Microcomputed tomography (μCT) was used to study in detail the 3D architectures of the printed porous hydrogels. To enhance the radiographic contrast, the purified scaffolds were first partially dehydrated using a 50:50 v/v water/ethanol solution for 5 min, washed in hexamethyldisilazane (Sigma-Aldrich) for other 5 min, and subsequently transferred to sunflower oil. The imaging process was performed using an Xradia MicroXCT-400 instrument, employing the following parameters: a voltage of 40 kV, power of 10 W, and a rotation step of 0.18° over an angle range of 184°. Scans were conducted at room temperature (25°C) and atmospheric pressure. The acquired data from μCT were analyzed using ImageJ software. Z-projections of

the samples were analyzed to determine the average pore size within the printed structures.[42]

4.2 | Culture of NIH/3T3 fibroblasts

Dulbecco's modified Eagle's medium (Thermo Fischer Scientific) (DMEM) containing 10% (v/v) fetal bovine serum (R&D Systems) (FBS) and 1% (v/v) antibiotic-antimycotic (Gibco) (anti-anti) was used as medium to culture NIH/3T3 fibroblasts (American Type Cell Culture). Cultivation was performed in T-175 tissue flasks (Sigma-Aldrich), which were put for cultivation in a humidified incubator (Nuaire) with a temperature of 37°C and a carbon dioxide (CO_2) concentration of 5% (v/v). The cells were checked for confluence and medium was change every 2 days. Once the cells had grown confluent, they were passaged to allow further growth.

4.3 | Cell seeding and characterizations

To harvest and seed the cells onto the 3D-printed porous structures, they were trypsinized as described. To determine the cell concentration of each tissue flask, cell counting was performed using an automated cell counter (Thermo Fischer Scientific). For cell seeding, porous cylindrical 3D-printed scaffolds with a thickness of 4 mm, a diameter of 5.4 mm were prepared. These were placed in one well each of a 24-well plate following the printing process described. To sterilize the samples for cell cultivation, they were placed under an UV lamp for 30 min. On each printed sample, 1×10^6 cells were placed. These were first incubated for 2 h at 37°C to allow the cells to adhere to the hydrogel structure. After 2 h, 1 mL of additional cell culture medium was added to each sample and incubation was continued. The cell culture medium of the samples was checked for change daily. Three biological replicates were prepared for each of the cell staining methods.

For live and dead staining, 1 mL of DPBS was prepared with 1-μL calcein acetoxymethylester (calcein-AM) (Thermo Fischer Scientific) and 1-μL ethidium homodimer-1 (Thermo Fischer Scientific). The samples to be analyzed were placed in a new 24-well plate and washed twice with DPBS. Then, 1 mL of the live and dead staining solution was added to each sample and incubated for 20 min. After two washes of the sample with DPBS, the sample was analyzed using a fluorescence microscope. Measurements are made on days 1, 3, 7, 10, and 14 with each day determined in triplicate.

For the F-actin and nuclei staining, cultivation medium of the sample was aspirated. After each step described below, the sample was washed twice with DPBS. After the first wash, the sample was covered with an aqueous 10% (v/v) formalin (Sigma-Aldrich) solution for 20 min at room temperature to fix it by stopping cell degradation processes. Then, a 0.3% (v/v) Triton X-100 (Sigma-Aldrich) solution in DPBS was added at room temperature to make the cell membrane permeable. This was allowed to act again for 20 min. In the next step, 1 mL of a 5% (w/v) bovine serum albumin (BSA) (Sigma-Aldrich) solution in DPBS was added to the sample to reduce nonspecific background staining. This requires a 2-h incubation in the cold room at 4°C on a shaker. 1 mL of the 0.25% (v/v) phalloidin staining solution (Sigma-Aldrich) in DPBS was then added to the sample and was left to act in the cold room for at least 16 h. In the final step, 4′,6-diamidine-2-phenylindole (DAPI) (Thermo Fischer Scientific) was added in a 0.1% (v/v) DPBS solution, which was allowed to soak for an additional 15 min. Measurements were made on days 1, 3, 7, 10, and 14 with each day determined in triplicate.

5 | RESULTS AND DISCUSSIONS

5.1 | Choice of surfactant

To stabilize the bubbles generated by the microfluidic chip, surfactants were utilized as they reduce the surface tension at the air-liquid interface. This prevents bubbles from collapsing or merging, ensuring consistent print quality and material properties. The 7.5% (w/v) fGelMA hydrogel was used to determine the best amount of one out of the three studied surfactants. The comparison of the three different surfactants and their resulting foam stability after 0, 2, and 5 min is shown in Figure S3. In all experiments, it could be noticed upon visual observation that after 0 and 2 min, a clear boundary between the foam and liquid phases had not yet formed, whereas this was the case after 5 min. Comparing the different surfactants with each other, rhamnolipids showed the poorest stabilization of the foam both at a concentration of 0.5% (w/v) and at 5% (w/v). In contrast, CTAB was shown to produce a more stable foam compared to lecithin at a concentration of 5% (w/v), but this was not the case at 0.5% (w/v). Here, lecithin seemed to exhibit the best results for 5 min of duration, which is sufficient time for printing under most scenarios. As a result, and due to the lower concentrations of lecithin that can be used for stabilization, further reducing its potential cytotoxicity, lecithin was chosen as the best surfactant. In addition, Figure S4 shows that a concentration of 1% (w/v) of lecithin was the most suitable among those tested (0%, 0.5%, 1%, 3%, or 5% (w/v)).

5.2 | Bubble size-control using the vFF chip

Since the orifice of the vFF chip is an important component for controlling on-demand the bubble size inside the chip, experiments were conducted regarding its pressure-dependence. For this purpose, only the second pressure input p_v of the vFF chip was connected to a tank with compressed air, which was adjusted using a digital manometer connected to an analog single-stage pressure-regulator. The quantitative pressure-dependence of the orifice is shown in Figure 2A presenting microscopic images of the orifice at different applied pressures p_v varying between 0, 1.0, 1.7, and 2.3 bar. It was found that the pressure-dependence of the orifice resembled an inverse sigmoid function, where the orifice was approximately 100-μm wide at atmospheric pressure. At an applied pressure of 2.3 bar, the orifice had completely closed and broke at pressures >2.5 bar.

Next, air bubbles of controllable sizes trapped within the polymer matrix were generated using the vFF chip. The results of robust bubble-generations are summarized in Figure 2B. Here, the inlet pressure p_g was set constant at 150 mbar for all four conditions using the pressure regulator, whereas the flow rates of the 7.5% (w/v) fGelMA and

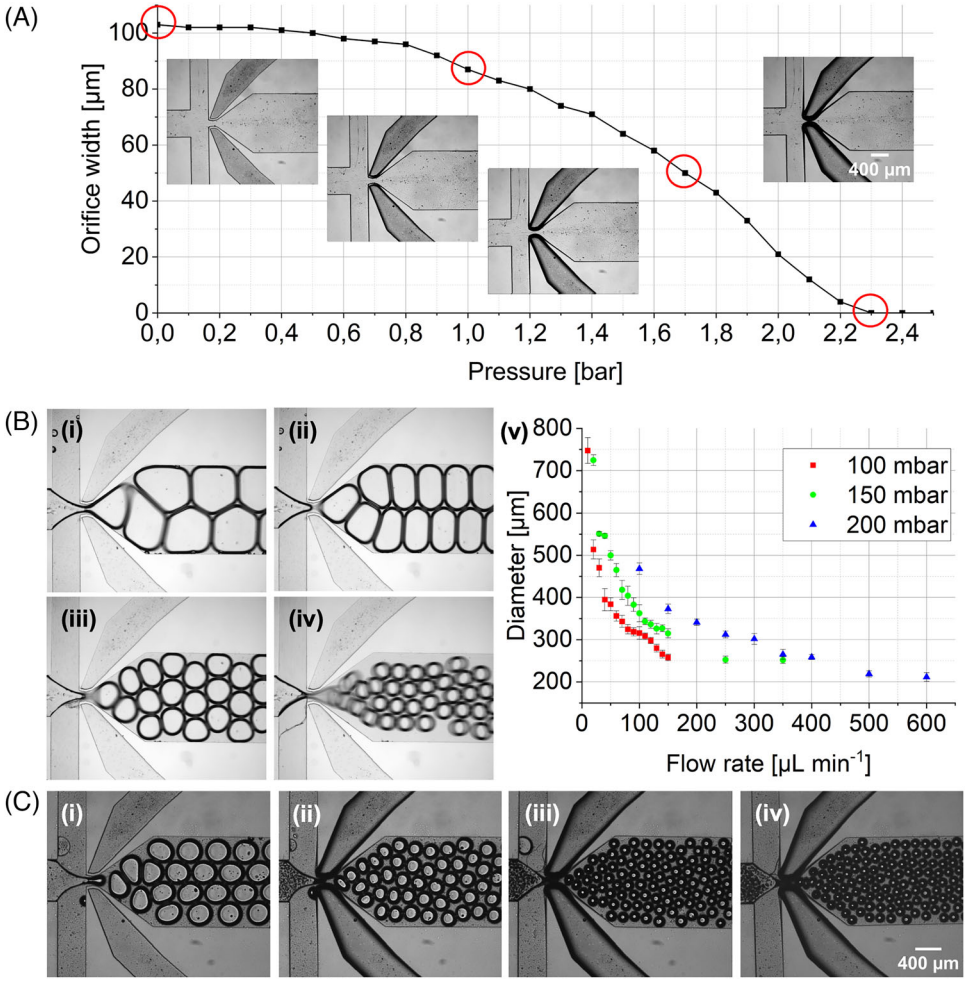

FIGURE 2 (A) Quantitative indication of the reduction of the orifice width of the valve-based flow-focusing (vFF) chip as a function of p_v = 0–2.5 bar. Microscope images of the orifice of the vFF chip at different pressures ranging from 0, 1.0, 1.7, to 2.3 bar. (B) Microscopic images on the controllability of the bubble sizes within the vFF chip at constant applied pressure p_g = 150 mbar and varying flow rates of the ink at 20, 30, 80, and 350 μL min^{-1}. P_v is constant at atmospheric pressure (i–iv). Quantification of average bubble sizes and their standard deviations as a function of flow rate at three different applied pressures p_g (v). (C) Further reduction of bubble size by applying a pressure p_v to the orifice of the vFF chip. Orifice pressure p_v variation ranging from 0 to 2.2 bar with resulting bubble sizes down to 143 ± 7 μm on average.

1% (w/v) lecithin ink were varied from 20 to 30, 80, and 350 μL min^{-1} (Figure 2B (i-iv)). The plot in Figure 2B (v) additionally highlights that a wide range of different combinations of pressures for p_g, as well as the volumetric flow rates of the ink, could be applied to robustly generate size-tunable bubbles with uniform diameters and small standard deviations. In these experiments, the pressure inlet p_v for the valve was set to atmospheric pressure to investigate the extent to which bubble sizes are limited downward without utilizing the orifice.

As shown in Figure 2B, bubbles with an average maximum diameter of approximately 747 ± 30 μm were generated using a volumetric flow rate of 10 μL min^{-1} and a pressure of p_g = 100 mbar. Similar average bubbles size of 725 ± 13 μm were generated with a volumetric flow rate of 20 μL min^{-1} and p_g = 200 mbar. Larger bubble diameters were not able to be generated at pressures above p_g = 200 mbar as the bubbles broke off due to the pressure-to-flow rate ratio being too large. Over the three series of experiments, it was possible to recognize the correlation that with an increasing pressure p_g and a certain target diameter, correspondingly higher flow rates were required. Across all experiments, it was shown that the bubble diameters at constant pressure p_g and as a function of the volumetric flow rate showed an exponential decay. The smallest average bubble diameter generated was 211 ± 10 μm at a pressure of 200 mbar and a volumetric flow rate of 600 μL min^{-1}. However, further increase in flow rate did not result in additional reduction of bubble sizes. Thus, it can be concluded that the reduction of bubbles diameters without the use of the orifice was capped to a lower limit, in this case 211 μm on average. For all diameter measurements made within the vFF chip, it must be noted that the bubbles were constrained by the height of the chip itself, resulting in a compression.

Within all presented samples, relative standard deviations in the range of approximately 3% were measured. The maximum deviation was 6.6%. Wider standard deviations tended to be observed for large bubble diameters. This was likely because the bubbles were not perfectly circular when they were formed inside the chip. In this case, horizontal and vertical diameters were measured when analyzing the data and the mean diameters were calculated from these, leading to higher deviations. However, it should be mentioned that only a limited number of combinations for pressures and flow rates were tested. Previous studies have shown that comparable results can be generated at lower pressures and flow rates using the same microfluidic chip and a similar setup.[22] It

therefore stands to reason that even higher process parameters can result in similar bubble diameters but in this case the bubbles are only formed at higher frequencies.

To further reduce the sizes of the generated bubbles and to break the lower limit of approximately 211 μm in average described before, the pressure-dependence of the orifice of the vFF chip on the bubble diameters was investigated. Figure 2C illustrates this schematically. During the acquisition of all images, the volumetric flow rate of the biopolymer was maintained constant at 100 μL min^{-1} whereas the inlet pressure p_g was set to 150 mbar. Furthermore, an additional pressure p_v was applied to the orifice of the chip. Such a pressure was increased from 0 to 2.2 bar. In addition to the pressures and the flow rate presented in Figure 2C, a variety of other combinations of these process parameters were tested out. This was done to demonstrate the robustness of bubble generation under different conditions. In total, the following combinations for the volumetric flow of the ink and for the inlet pressure p_g were successfully tested: 50 μL min^{-1} at 100 mbar, 50 μL min^{-1} at 150 mbar, 100 μL min^{-1} at 100 mbar, 100 μL min^{-1} at 150 mbar, and 100 μL min^{-1} at 200 mbar. For all these combinations, the pressure p_v was increased to a maximum value of 2.2 bar. Here, similar trends as shown in Figure 2B were observed for all combinations although there were minor deviations with respect to the resulting bubble diameters. In the case shown in Figure 2C, the following results for average bubble diameters and their standard deviations were obtained: (i) 367 ± 12 μm, (ii) 243 ± 11 μm, (iii) 159 ± 6 μm, and (iv) 143 ± 7 μm.

As can be seen from the reduction in the bubble size with increasing pressure p_v, the bubbles became increasingly smaller rapidly, especially at the higher pressures p_v. This observation suggested that the reduction in bubble diameter was not linear with pressure p_v. As expected, it was thus confirmed that the size of the bubbles could be further reduced beyond the previously described lower limit with the help of the orifice. In summary, the size of the bubbles inside the vFF chip was able to be controlled in a robust process and with a variability of different process parameters in the range of 747 μm down to 143 μm.

6 | 2D PRINTABILITY

A photoinitiator was added to the previously described ink formulation to enable its chemical crosslinking and thus 2D and 3D printability. For this purpose, inks containing LAP with varying concentrations were prepared and evaluated for photocrosslinking at different light exposure times. The results are shown in Figure S5. A concentration of 1% (w/v) LAP was used for further experiments since this enabled robust and reproducible crosslinking with less than 15 s of exposure time at 405-nm light.

To illustrate the basic operation of DLP printing, geometries of increasing complexity were 2D-printed first, as illustrated in Figure 3A. In the upper row, five slices from different computer-aided design (CAD) files are shown. The five 2D-printed geometries had a bone-like structure, a curved channel, a honeycomb, a leaf, and a vascular network. In the middle row, photographic images of the actual 2D-printed geometries are shown. These were made with the described ink formulation (7.5% (w/v) fGelMA, 1% (w/v) lecithin, 1% (w/v) LAP). The volumetric flow rate inside the vFF chip was 650 μL min^{-1} with pressures p_g = 1.3 bar and p_v = atmospheric pressure. The generated foam pattern was situated on a glass slide and photocrosslinked. After crosslinking, all samples were rinsed with DI water and then photographed. In the lower row (Figure 3A (iii)), high-resolution images of the geometries were taken using a bright-field microscope. In this illustration of different 2D prints, the bubble size had intentionally not been controlled yet. Although fundamentally different geometries were printed, all process parameters were kept the same and did not need to be further optimized depending on the geometry. In addition, printing time was independent of the complexity of the structure itself.

Furthermore, 2D prints with precisely tuned bubble diameters were produced. Figure 3B schematically illustrates the printing of bone-like structures on a glass slide. Hereby, the diameters of the 2D-printed gas bubbles increased with each condition as revealed in the bottom magnified ones. Figure 3B shows the variation in bubble size across five different bubble sizes. The images were acquired using a bright-field microscope. The presented bubble sizes were quantified and histograms representing their size distributions were constructed. In contrast to Figure 3A, a constant volumetric flow rate of 50 μL min^{-1} was applied across all five conditions during the experiments shown here. The pressure p_g was varied between 100 to 250 mbar and the pressure p_v was varied between 0 and 2.25 bar. Using these process parameters, gas bubbles with average diameters of 112 ± 7, 198 ± 7, 239 ± 19, 361 ± 17, and 424 ± 17 μm were printed in 2D (see histograms). Further characteristic values related to the histograms are recorded in Table S1. Looking at the size distributions, as the bubble diameter was elevated, the deviation around the mean value increased as well and the distribution therefore became wider, consistent with data without printing. It was also observed that the bubbles produced using the vFF chip in these experiments could reach an average maximum diameter of 424 μm whereas the largest bubbles within the vFF chip reached diameters of up to 747 μm in average (Figure 3B). This effect can be attributed to the fact that the bubbles outside the chip are no longer compressed by the height of the chip and thus become three-dimensionally circular instead of ellipsoidal, which reduces their diameters. Furthermore, it was observed that the larger bubbles tended to be less stable once they were at atmospheric pressure outside of the chip which partly led to the collapse of the bubbles. For all bubble sizes in Figure 3B, it was observed that the generated gas bubbles were highly circular. Furthermore, it was observed that the bubbles arranged forming close-packed hexagonal crystal patterns on a planar surface such as the glass slides used.

From here, the extent to which 2D pore size gradients could be printed was tested, since this can be of particular interest for the application of gradients in 3D, for example to reproduce axial porosities along a bone. As an example, results are shown in Figure 3C in which gradients in bubble sizes were printed in a single 2D print without interruption due to the rapid digital control directly applicable on the vFF chip. Figure 3C shows the corresponding microscopic images. Here, the micrographs show homogeneous bubble sizes as well as the transitions to smaller ones going from left to right. While the large-sized bubbles were prepared

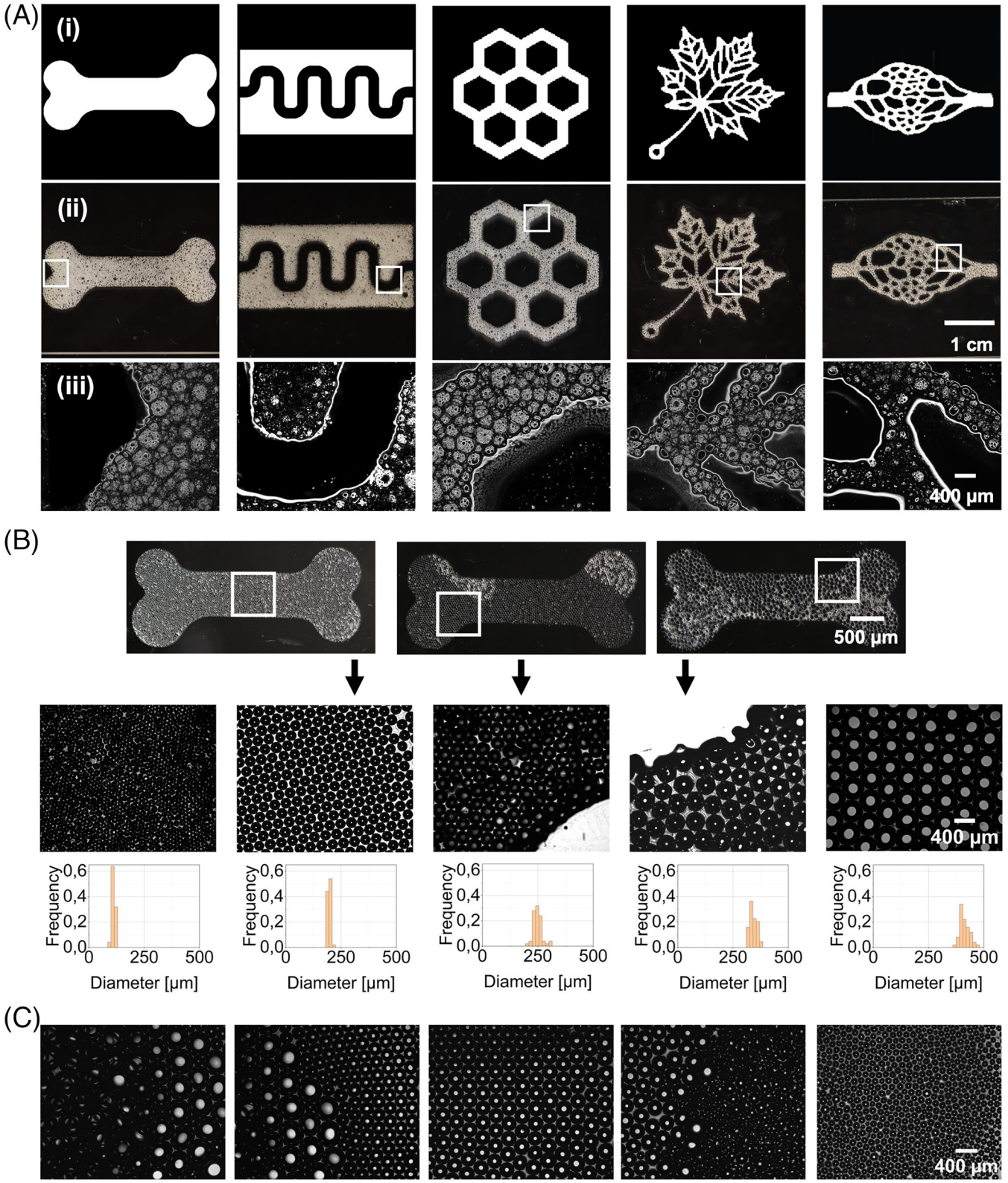

FIGURE 3 (A) Computer-generated 2D shapes of varying complexity for the schematic representation of single-layer print utilizing a digital light processing (DLP) printer (i); 2D-printed shapes (ii); zoom-in micrographs of the 2D-printed shapes and illustration of the generated bubbles (iii). (B) 2D-printed porous bone-like structures with controlled bubble sizes. Microscopic images of five different bubble sizes ranging from 112 to 424 μm in average. Histograms of five different bubble sizes with $n > 40$ measurements each. (C) 2D-printed bubble size gradients showing the generation of size-tunable small-, medium-, and large-sized bubbles.

with a biopolymer volumetric flow rate of 50 μL min^{-1} and pressures of $p_g = 250$ mbar and p_v = atmospheric pressure, the pressure was reduced to $p_g = 100$ mbar for the medium-sized bubbles. For the small-size bubbles, the pressure p_v was additionally increased to 2.25 bar to narrow the orifice of the vFF chip. Again, highly uniform circular bubbles with mostly hexagonal packing alignments were observed after crosslinking of the ink.

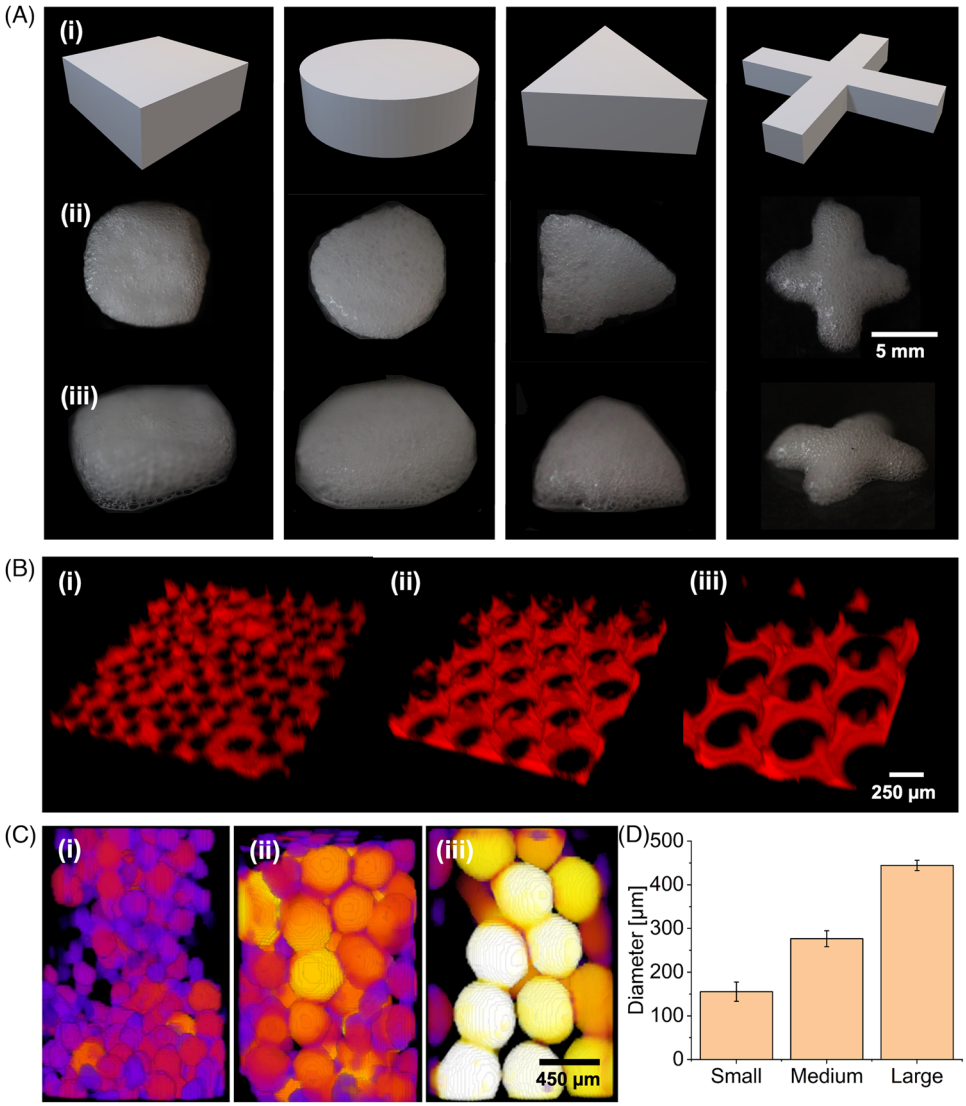

FIGURE 4 (A) Computer-aided design (CAD) designs for 3D digital light processing (DLP) printing (i). Top view of the 3D-printed porous constructs using the top-down DLP printer (ii). Side views of these patterns (iii). Each pattern had a total height of 4 mm at 20 layers, 200 μm per layer, and 5 s of 405-nm light exposure time per layer. (B) Confocal fluorescence micrographs showing the spatial morphologies of single-layer small (i), medium (ii), and large (iii)-sized gas bubbles trapped in a rhodamine-conjugated fGelMA hydrogel. (C) μCT scans of small (i), medium (ii), and large (iii)-sized bubbles as well as (D) their quantified average sizes and standard deviations.

7 | 3D DLP PRINTABILITY

By using a top-down DLP printer, it was possible to obtain reproducible printing results with the foam inks. It was shown that the top-down printer was particularly advantageous for generating soft and fragile objects as it is the case here, since weaker external forces act on the those unlike the gravitational force and other forces in the bottom-up printer that may break the structure during 3D printing.[31] Figure 4A shows the 3D printing results of geometries with increasing complexity. Figure 4A (i) illustrates 3D CAD designs of a cube, a cylinder, a triangle, and a cross, while. Figure 4A (ii) and (iii) shows the print results in top- and side-view. For each sample, the final printing parameters are summarized in Table 1. The 3D structures printed demonstrated their stability towards applications as cell scaffolds. After being immersed in cell culture medium for 14 days, the printed scaffolds could still maintain their structural integrity without showing noticeable deformations. The stability of the printed constructs could be further adjusted by modulating the properties of GelMA used for 3D printing.[43]

Although the print results shown were reproducible, they were still not entirely optimal and offered room for future improvement. For example, it was observed that the 3D resolution of the prints was not high enough to print sharp edges. Besides the already described limitations by the bubble size itself (Figure S6), relatively high LAP concentration could have further led to an over-crosslinking of the hydrogel and therefore to a reduction of the spatial resolution.[44] Additionally, it can be seen from the images that the surface of the 3D-printed structures was not perfectly planar. One challenge during the printing process was that the printing stage had to be adjusted to the correct height one layer thickness below the surface of the foam where surface tension would lead to uneven printing results.

The spatial architecture of the porous structures was examined first by using confocal fluorescence microscopy in combination with rhodamine-conjugated fGelMA. For the

TABLE 1 Final process parameters for the generation of bubbles inside the valve-based flow-focusing (vFF) chips as well as the printing parameters applied at the top-down digital light processing (DLP) printing system.

vFF bubble-generation parameters (unit)			Top-down DLP printing parameters (unit)			
P_g (bar)	P_v (bar)	Ink flowrate (μL min^{-1})	Exposure time (s)	Layer height (μm)	Number of projected layers (-)	Speed (mm s^{-1})
0.1-0.25	0-2.25	50	5	200	20	0.1

confocal microscope scans, samples with different bubble diameters were placed in-between two glass slides with 750-μm-thick spacers and subsequently crosslinked under UV light. The resulting 3D confocal images are shown in Figure 4B. As was already the case with the images of the 2D prints, confocal analysis revealed that the gas bubbles arranged themselves according to the hexagonally densest sphere packing. Moreover, the confocal images revealed that most of the generated pores were already interconnected in their 3D arrangement. The Kepler conjecture suggests that the porosity of constructs, determined by the ratio of void volume to total volume, becomes independent of sphere radius in a theoretical hexagonal or cubic close sphere packing. This potentially reaches a maximum porosity of approximately 74%, although practical deviations may occur.

Comparing the results obtained in the confocal analysis of our structures with the conventional approach of using microspheres as templates to generate void volumes within a polymer matrix,[16-19,45] one limitation is the secondary removal process of the porogen, which however, is not needed here due to the hollow nature of the air bubbles adopted in our foam inks. Thus, it can be concluded that the microfluidic bubble-generation chip-enhanced 3D DLP printing method presented here was able to allow production of pore diameters with good uniformity, a wider range of achievable diameters, and with a more controllable and faster process.

To gain a better understanding of the internal nature of the 3D-printed samples as they would be in a non-ideal, real-world environment, μCT reconstructions of these were performed. Again, for simplicity, samples with small-, medium-, and large-sized pore diameters were produced. The results are summarized in Figure 4C. It was observed that, unlike in the images from the confocal fluorescence microscope, these constructs showed some reduction in porosity, that is, the bubbles were not perfectly arranged anymore. There could be different reasons behind such an observation. On the one hand, when printing in 3D the surface tension and other operations during printing might have caused defects to form resulting in nonperfect close packing of the bubbles in the foam ink. On the other hand, handling during sample-preparation for the μCT scans may have resulted in the structures being negatively affected by external forces. Nevertheless, the μCT scans confirmed once again that the generated porous structures were precisely adjustable.

7.1 | Postprocessing and 3D culture of NIH/3T3 fibroblasts

Porous fGelMA constructs were printed as described above, sterilized using a UV lamp for 30 min in a 24-well plate, and fibroblasts were then seeded onto the scaffolds. In this process, 1×10^6 cells in 100 μL of cell culture medium were placed on top of each construct. This post-seeding procedure was carried out for several reasons. For example, no shear forces acted on the cells which would be the case if they were encapsulated in the fGelMA hydrogel from the start and passed through the microfluidic vFF chip channels. Furthermore, the time in contact with potentially cytotoxic drying conditions within the foam where a large amount of air is present, was reduced significantly, as well as the negative impacts exerted by prolonged exposure to the relatively high concentrations of lecithin and LAP needed for stabilizing the bubbles and for efficient photocrosslinking, respectively. Besides the avoided irradiation of the fibroblasts with light with a wavelength of 405 nm, the possible sterile handling of the hydrogel can also be mentioned as a further advantage.

The cytocompatibility of the 3D-printed porous hydrogel constructs with cells seeded in them is essential for the long-term goal of tissue-replacement when it comes to applications in tissue engineering and regenerative medicine. Based on that, cell viability, proliferation, migration, and spreading were investigated qualitatively by various staining methods. To this end, the cells were cultured in the 3D-printed porous constructs first with uncontrolled pore sizes for 14 days, where live/dead assays as well as F-actin/nuclei staining were conducted in triplicates at 1, 3, 7, 10, and 14 days (Figure 5A and B). In addition, samples of different types were prepared for a 7-day cultivation of NIH/3T3 fibroblasts followed by live/dead staining, in which case the porous constructs exhibited precisely defined pore sizes with narrow size distributions as described (Figure 5C).

Throughout the entire cultivation period of 14 days, it was observed that a high degree of cytocompatibility for the used bioink was the case. The percentages of dead cells were low at all the time points evaluated, with cell viabilities of >95% semiquantified from the images. Morphologically, on day 1, the cells were arranged in clusters with a rounded appearance, indicating that no considerable cell spreading occurred, yet. Starting from cultivation at day 3 until the end of cultivation, gradual cell attachment to the surfaces between the pores was noticeable. Simultaneously, it was observed that the cell density within the 3D-printed porous constructs increased with each time point of cultivation we evaluated. While many areas of the hydrogel scaffolds without any cells were still visible on the day 1, the constructs were significantly more populated on day 14, with the cells occupying most of the sample surface. Cell spreading, proliferation, or/and migration were further validated with F-actin/nuclei staining. Accordingly, it can be assumed that the 3D-printed porous fGelMA constructs enabled proper cell behaviors within the pores, also with its pore structure remaining intact over 2 weeks of culture not showing noticeable collapse due to the high porosity.

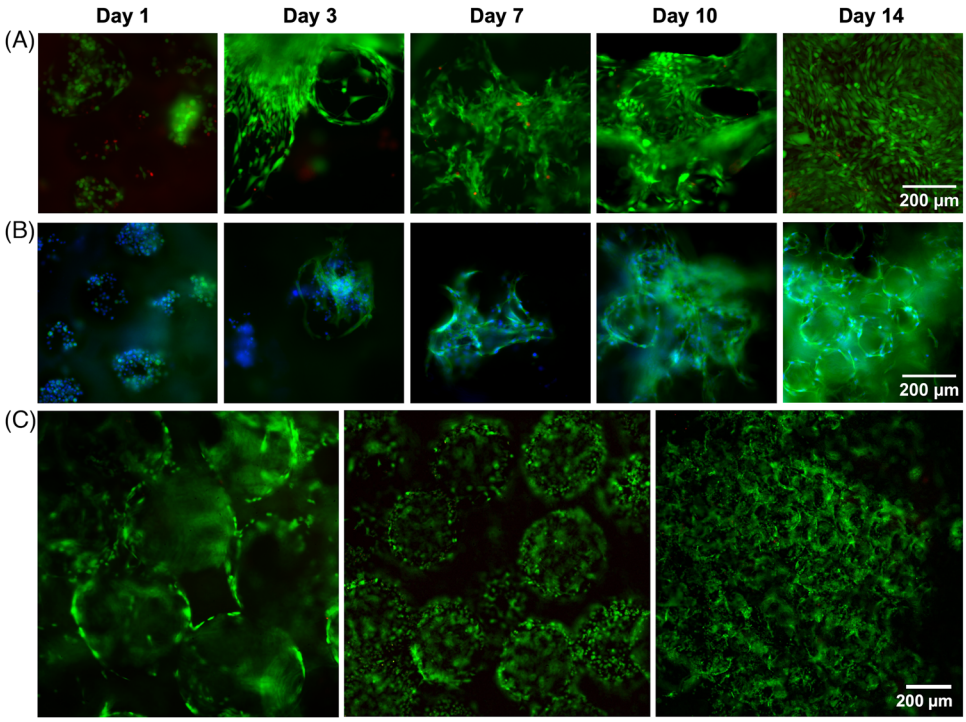

FIGURE 5 (A) Fluorescence micrographs qualitatively showing the high cell viability of seeded NIH/3T3 fibroblasts after 1, 3, 7, 10, and 14 days of cultivation in porous constructs printed from fGelMA and lecithin-stabilized inks without bubble size-control, showing the overlay of live (green) and dead (red) cells. (B) Morphology of NIH/3T3 fibroblasts after 1, 3, 7, 10, and 14 days of cultivation in porous constructs printed from fGelMA and lecithin-stabilized inks without bubble size-control, showing their F-actin filaments (green) and nuclei (blue). (C) Live (green) and dead (red) staining of fibroblasts in porous scaffolds with precisely controlled (large-, medium-, and small-sized) bubbles after 7 days of cultivation.

8 | CONCLUSIONS

In summary, this study aimed to develop a proof of concept for 3D printing of porous, soft hydrogels equipped with a bubble-generating microfluidic chip, advancing tissue engineering platforms. It was demonstrated how to create size-adjustable porosities with narrow size distributions within 3D-printed constructs for enhanced mimicry of native porous tissues. A top-down DLP printer was selected, and a robust printing process was established. Cytocompatibility tests were conducted on a specially formulated ink using various cell staining assays, where it was demonstrated that the porous constructs supported cell growth, spreading, proliferation, and migration over a 14-day period. The use of fGelMA as the ink material for DLP printing was favored due to its physicochemical properties. An aqueous 7.5% (w/v) fGelMA solution was chosen, and lecithin at 1% (w/v) was found to be the most effective foam stabilizer among the tested surfactants. A 1% (w/v) LAP concentration served as the photoinitiator for chemical crosslinking of the foam. By adjusting ink flow rate and gas pressures, control over gas bubble sizes was achieved, with uniform diameters ranging from as large as 747 μm to as small as 143 μm demonstrated in the current study. Overall, the work successfully achieved the generation of size-tunable uniform gas bubbles within a hydrogel matrix, to manufacture cytocompatible, porous scaffolds.

Nevertheless, the technology does not come without limitations. First, further research efforts will be required to extend the duration of bubble stability sufficiently for DLP printing of larger structures. Moreover, to overcome the challenges with regard to the 3D printing resolution, several attempts can be tested for further improvements. For example, by optimizing the light source and the optical system setup, better resolutions might be achieved. Furthermore, process parameters such as the projected pixel size, the layer height, as well as the light exposure time can all be fine-tuned specifically for this application of 3D DLP printing of porous structures. Additional possibilities would include post-printing resolution-enhancement.[46] With these additional optimizations, the developed microfluidic application will likely expand the capabilities of DLP printers used towards broad applications.

ACKNOWLEDGMENTS

M.C., M.C.T., and W.S. acknowledge funding support from the National Science Centre Poland (NCN) within OPUS 19 project number: 2020/37/B/ST8/02167. F.N. acknowledges funding from the European Union's Horizon 2020 research and innovation program under the Marie Sklodowska-Curie grant agreement number: 813786 (EVOdrops). YSZ acknowledges support from the National Institutes of Health (grant number: R21EB025270), National Science Foundation (grant number: CBET-EBMS-1936105), and the Brigham Research Institute.

CONFLICT OF INTEREST STATEMENT

The authors declare no conflict of interest.

ORCID

Maria Celeste Tirelli https://orcid.org/0000-0002-6670-4014
Marco Costantini https://orcid.org/0000-0003-2756-5872
Yu Shrike Zhang https://orcid.org/0000-0002-0045-0808

REFERENCES

1. S.V. Murphy, A. Atala, *Nat. Biotechnol.* **2014**, *32*, 773.
2. M. Mobaraki, M. Ghaffari, A. Yazdanpanah, Y. Luo, D. Mills, *Bioprinting* **2020**, *18*, e00080.
3. Y. S. Zhang, R. Oklu, M. R. Dokmeci, A. Khademhosseini, *Cold Spring Harb. Perspect. Med.* **2018**, *8*, a025718.
4. D. Huh, G. A. Hamilton, D. E. Ingber, *Trends Cell Biol.* **2011**, *21*, 745.
5. S. Caddeo, M. Boffito, S. Sartori, *Front. Bioeng. Biotechnol.* **2017**, *5*, 40.
6. L. Moroni, J. A. Burdick, C. Highley, S. J. Lee, Y. Morimoto, S. Takeuchi, J. J. Yoo, *Nat. Rev. Mater.* **2018**, *3*, 21.
7. S.-W. Choi, Y. Zhang, Y. Xia, *Langmuir* **2010**, *26*, 19001.
8. F. J. Maksoud, M. F. V. d. l. Paz, A. J. Hann, J. Thanarak, G. C. Reilly, F. Claeyssens, N. H. Green, Y. S. Zhang, *J. Mater. Chem. B* **2022**, *10*, 8111.
9. S. B. Farid, *Bioceramics: for materials science and engineering*, Woodhead Publishing, Sawston, UK, **2018**.
10. T. Mays, *Stud. Surf. Sci. Catal.* **2017**, *160*, 57.
11. E. Babaie, S. B. Bhaduri, *ACS Biomater. Sci. Eng.* **2018**, *4*, 1.
12. N. Abbasi, S. Hamlet, R. M. Love, N.-T. Nguyen, *J. Sci.: Adv. Mater. Devices* **2020**, *5*, 1.
13. S. D. Lacey, D. J. Kirsch, Y. Li, J. T. Morgenstern, B. C. Zarket, Y. Yao, J. Dai, L. Q. Garcia, B. Liu, T. Gao, S. Xu, S. R. Raghavan, J. W. Connell, Y. Lin, L. Hu, *Adv. Mater.* **2018**, *30*, 1705651.
14. A. Limper, N. Weber, A. Brodersen, R. Keller, M. Wessling, J. Linkhorst, *Electrochem. Commun.* **2022**, *134*, 107176.
15. L. C. Hwa, S. Rajoo, A. M. Noor, N. Ahmad, M. Uday, *Curr. Opin. Solid State Mater. Sci.* **2017**, *21*, 323.
16. D. Huang, T. Liu, J. Liao, S. Maharjan, X. Xie, M. Perez, I. Anaya, S. Wang, A. T. Mayer, Z. Kang, W. Kong, V. L. Mainardi, C. E. Garciamendez-Mijares, G. G. Martinez, M. Moretti, W. Zhang, Z. Gu, A. M Ghaemmaghami, Y. S. Zhang, *Proc. Natl. Acad. Sci.* **2021**, *118*, e2016146118.
17. S.-W. Choi, Y. S. Zhang, M. R. MacEwan, Y. Xia, *Adv. Healthc. Mater.* **2013**, *2*, 145.
18. Y. S. Zhang, C. Zhu, Y. Xia, *Adv. Mater.* **2017**, *29*, 1701115.
19. B. A. Dikici and F. Claeyssens, *Front. Bioeng. Biotechnol.* **2020**, *8*, 875.
20. X. Mu, T. Bertron, C. Dunn, H. Qiao, J. Wu, Z. Zhao, C. Saldana, H. J. Qi, *Mater. Horiz.* **2017**, *4*, 442.
21. Z. Dong, H. Cui, H. Zhang, F. Wang, X. Zhan, F. Mayer, B. Nestler, M. Wegener, P. A. Levkin, *Nat. Commun.* **2021**, *12*, 247.
22. M. Costantini, J. Jaroszewicz, Ł. Kozoń, K. Szlązak, W. Święszkowski, P. Garstecki, C. Stubenrauch, A. Barbetta, J. Guzowski, *Angew. Chem. Int. Ed.* **2019**, *58*, 7620.
23. M. Marcotulli, M. C. Tirelli, M. Volpi, J. Jaroszewicz, C. Scognamiglio, P. Kasprzycki, K. Karnowski, W. Święszkowski, G. Ruocco, M. Costantini, G. Cidonio, A. Barbetta, *Adv. Mater. Technol.* **2023**, *8*, 2201244.
24. Y. S. Zhang, G. Haghiashtiani, T. Hübscher, D. J. Kelly, J. M. Lee, M. Lutolf, M. C. McAlpine, W. Y. Yeong, M. Zenobi-Wong, J. Malda, *Nat. Rev. Dis. Primers.* **2021**, *1*, 75.
25. C. Yu, J. Schimelman, P. Wang, K. L. Miller, X. Ma, S. You, J. Guan, B. Sun, W. Zhu, S. Chen, *Chem. Rev.* **2020**, *120*, 10695.
26. R. J, Mondschein, A. Kanitkar, C. B. Williams, S. S. Verbridge, T. E. Long, *Biomaterials* **2017**, *140*, 170.
27. A. Bagheri, J. Jin, *ACS Appl. Polym. Mater.* **2019**, *1*, 593.
28. Y. Bao, N. Paunović, J. C. Leroux, *Adv. Funct. Mater.* **2022**, *32*, 2109864.
29. W. Li, M. Wang, H. Ma, F. A. Chapa-Villarreal, A. O. Lobo, Y. S. Zhang, *iScience* **2023**, *26*, 106039.
30. W. L. Ng, J. M. Lee, M. Zhou, Y.-W. Chen, K.-X. A. Lee, W. Y. Yeong, Y.-F. Shen, *Biofabrication* **2020**, *12*, 022001.
31. W. Li, L. S. Mille, J. A. Robledo, T. Uribe, V. Huerta, Y. S. Zhang, *Adv. Healthc. Mater.* **2020**, *9*, 2000156.
32. A. K. Miri, D. Nieto, L. Iglesias, H. G. Hosseinabadi, S. Maharjan, G. U. Ruiz-Esparza, P. Khoshakhlagh, A. Manbachi, M. R. Dokmeci, S. Chen, S. R. Shin, Y. S. Zhang, A. Khademhosseini, *Adv. Mater.* **2018**, *30*, 1800242.
33. M. Wang, W. Li, L. S. Mille, T. Ching, Z. Luo, G. Tang, C. E. Garciamendez-Mijares, A. Lesha, M. Hashimoto, Y. S. Zhang, *Adv. Mater.* **2022**, *34*, 2107038.
34. J. Liu, H. H. Hwang, P. Wang, G. Whang, S. Chen, *Lab Chip* **2016**, *16*, 1430.
35. G. Ying, N. Jiang, C. Parra-Cantu, G. Tang, J. Zhang, H. Wang, S. Chen, N.-P. Huang, J. Xie, Y. S. Zhang, *Adv. Funct. Mater.* **2020**, *30*, 2003740.
36. R. Levato, K. S. Lim, W. Li, A. U. Asua, L. B. Peña, M. Wang, M. Falandt, P. N. Bernal, D. Gawlitta, Y. S. Zhang, T. B. Woodfield, J. Malda, *Mater. Today Bio.* **2021**, *12*, 100162.
37. Q. Liu, L. S. Mille, C. Villalobos, I. Anaya, M. Vostatek, S. Yi, W. Li, J. Liao, H. Wu, Y. Song, L. Xiong, Y. S. Zhang, *Biodes. Manuf.* **2023**, *6*, 373.
38. L. Shao, R. Hou, Y. Zhu, Y. Yaoa, *Biomater. Sci.* **2021**, *9*, 6763.
39. M. Wang, W. Li, J. Hao, A. Gonzales III, Z. Zhao, R. S. Flores, X. Kuang, X. Mu, T. Ching, G. Tang, Z. Luo, C. E. Garciamendez-Mijares, J. K. Sahoo, M. F. Wells, G. Niu, A. Prajwal Agrawal, *Nat. Commun.* **2022**, *13*, 3317.
40. A. Mata, A. J. Fleischman, S. Roy, *J. Micromech. Microeng.* **2006**, *16*, 276.
41. Y. Xia, G. M. Whitesides, *Annu. Rev. Mater. Sci.* **1998**, *28*, 152.
42. M. Constantini, J. Guzowski, P. J. Zuk, P. Mozetic, S. De Panfilis, J. Jaroszewicz, M. Heljak, M. Massimi, M. Pierron, M. Trombetta, M. Dentini, W. Święszkowski, A. Rainer, P. Garstecki, A. Barbetta, *Adv. Funct. Mater.* **2018**, *28*, 1800874.
43. G. Ying, N. Jiang, C. Yu, Y. S. Zhang, *Biodes. Manuf.* **2018**, *1*, 215.
44. H. Lin, D. Zhang, P. G. Alexander, G. Yang, J. Tan, A. W.-M. Cheng, R. S. Tuan, *Biomaterials* **2013**, *34*, 331.
45. L. Ouyang, J. P. Wojciechowski, J. Tang, Y. Guo, M. M. Stevens, *Adv. Healthc. Mater.* **2022**, *11*, 2200027.
46. J. Gong, C. C. L. Schuurmans, A. M. van Genderen, X. Cao, W. Li, F. Cheng, J. J. He, A. López, V. Huerta, J. Manríquez, R. Li, H. Li, C. Delavaux, S. Sebastian, P. E. Capendale, H. Wang, J. Xie, M. Yu, R. Masereeuw, T. Vermonden, Y. S. Zhang, *Nat. Commun.* **2020**, *11*, 1267.

SUPPORTING INFORMATION

Additional supporting information can be found online in the Supporting Information section at the end of this article.

How to cite this article: P. Weber, L. Cai, F. J. A. Rojas, C. E. Garciamendez-Mijares, M. C. Tirelli, F. Nalin, J. Jaroszewicz, W. Święszkowski, M. Costantini, Y. S. Zhang, *Aggregate* **2024**, *5,* e409. https://doi.org/10.1002/agt2.409